

---

This is an electronic reprint of the original article.  
This reprint may differ from the original in pagination and typographic detail.

Sun, Kewei; Silveira, Orlando J.; Saito, Shohei; Sagisaka, Keisuke; Yamaguchi, Shigehiro;  
Foster, Adam S.; Kawai, Shigeki

## Manipulation of Spin Polarization in Boron-Substituted Graphene Nanoribbons

*Published in:*  
ACS Nano

*DOI:*  
[10.1021/acsnano.2c04563](https://doi.org/10.1021/acsnano.2c04563)

Published: 26/07/2022

*Document Version*  
Peer-reviewed accepted author manuscript, also known as Final accepted manuscript or Post-print

*Please cite the original version:*  
Sun, K., Silveira, O. J., Saito, S., Sagisaka, K., Yamaguchi, S., Foster, A. S., & Kawai, S. (2022). Manipulation of Spin Polarization in Boron-Substituted Graphene Nanoribbons. *ACS Nano*, 16(7), 11244–11250.  
<https://doi.org/10.1021/acsnano.2c04563>

---

This material is protected by copyright and other intellectual property rights, and duplication or sale of all or part of any of the repository collections is not permitted, except that material may be duplicated by you for your research use or educational purposes in electronic or print form. You must obtain permission for any other use. Electronic or print copies may not be offered, whether for sale or otherwise to anyone who is not an authorised user.

# Manipulation of Spin Polarization in Boron-Substituted Graphene Nanoribbons

*Kewei Sun<sup>1</sup>, Orlando J. Silveira<sup>2</sup>, Shohei Saito<sup>3</sup>, Keisuke Sagisaka<sup>1</sup>, Shigehiro Yamaguchi<sup>4</sup>, Adam S. Foster<sup>\*2,5</sup>, Shigeki Kawai<sup>\*1,6</sup>*

*<sup>1</sup>Research Center for Advanced Measurement and Characterization, National Institute for Materials Science, 1-2-1 Sengen, Tsukuba, Ibaraki 305-0047, Japan.*

*<sup>2</sup>Department of Applied Physics, Aalto University, PO Box 11100, FI-00076 Aalto, Finland.*

*<sup>3</sup>Graduate School of Science, Kyoto University, Kyoto 606-8502, Japan.*

*<sup>4</sup> Department of Chemistry, Graduate School of Science, Nagoya University, Furo, Chikusa, Nagoya 464-8602, Japan.*

*<sup>5</sup>WPI Nano Life Science Institute (WPI-NanoLSI), Kanazawa University, Kakuma-machi, Kanazawa 920-1192, Japan.*

*<sup>6</sup>Graduate School of Pure and Applied Sciences, University of Tsukuba, Tsukuba 305-8571, Japan.*

**ABSTRACT:** The design of magnetic topological states due to the spin polarization in an extended  $\pi$  carbon system has great potential in spintronics application. Although magnetic zigzag edges in graphene nanoribbons (GNRs) have been investigated, real-space observation and manipulation of the spin polarization in a heteroatom substituted system remains challenging. Here, we investigate a zero-bias peak at a boron site embedded at the center of the armchair-type GNR on a  $\text{AuSi}_x/\text{Au}(111)$  surface with a combination of low-temperature scanning tunneling microscopy/spectroscopy and density functional theory calculations. After the tip-induced removal of a Si atom connected to two adjacent boron atoms, a clear Kondo resonance peak appeared and was further split by an applied magnetic field of 12 T. This magnetic state can be relayed along the longitudinal axis of the GNR by sequential removal of Si atoms.

**KEYWORDS:** boron substituted graphene nanoribbons, silicon atoms,  $\text{AuSi}_x$  layer, scanning tunneling microscopy/spectroscopy, spin polarization, Kondo resonance.

## INTRODUCTION

A magnetic state induced by spin polarization of  $\pi$ -electrons in graphene has attracted tremendous interest of researchers as a key element in spintronics.<sup>1,2</sup> For unambiguous characterization, it is of central importance to employ atomically defined extended polycyclic aromatic hydrocarbons (PAHs). To synthesize such PAHs, on-surface reactions are a powerful bottom-up method<sup>3,4</sup> since their structures can be precisely defined with designer precursors.<sup>5-7</sup> So far, several GNRs<sup>8-13</sup> and nanographenes<sup>14-20</sup> were found to host spin polarized states with most of them relying on zigzag edges to induce a local net spin.<sup>1,8,11-15,21</sup> Besides the physical edges, Pascual *et al.*, recently found that boron substitution in a GNR (B-GNR) gives a pair of apparent zigzag edges by the rupture of the conjugated system, consequently leading to a Kondo resonance in the vicinity of the boron sites.<sup>22</sup> Since the magnetic state is completely quenched by the strong adsorption to the Au(111) substrate,<sup>23</sup> the measurement was conducted by lifting a single B-GNR up from the surface as the boron site was partially detached.<sup>22</sup> To realize this measurement setup, a diluted B-GNR was used,<sup>24</sup> otherwise strong adsorption to the substrate at the boron site prevents the manipulation.<sup>25</sup> Nevertheless, the magnetism induced by the imbalance of  $\pi$ -electrons in real space cannot be measured in the tip-GNR-Au(111) transport configuration, thus their spatial distribution is still unclear.

Here, we investigate the magnetic states in B-GNR on an AuSi<sub>x</sub> intercalation layer formed on the Au(111) substrate. Deposited Si atoms adsorbed at the centers of two boron atoms in B-GNR, leading to the formation of one-dimensional Si arrays. We found that the magnetic state of a pair of boron atoms was recovered by removing the adsorbed Si atom with the tip of a scanning tunneling microscope (STM) and/or by contacting the Si tip at the boron sites.

## RESULTS AND DISCUSSION

Since the electronic property of B-GNR is significantly modulated by the strong adsorption to the Au(111) substrate,<sup>26</sup> we initially attempted to form a AuSi<sub>x</sub> intercalation layer for electrical decoupling (Figure 1a).<sup>27,28</sup> B-GNRs were first synthesized on a clean Au(111) by depositing 9,10-bis(10-bromoanthracen-9-yl)-9,10-dihydro-9,10-diboraanthracene (1) molecules and subsequently annealing at 180 °C for debromination and 320 °C for cyclodehydrogenation, respectively. We found a  $1.35 \pm 0.01$  nm spaced periodic modulation along the longitudinal axis of GNR in the STM topography (Figure 1b), which is in agreement with previous works.<sup>23</sup> To form the AuSi<sub>x</sub> layer between B-GNRs and the Au(111) substrate, Si atoms were *in situ* deposited on the substrate kept at 150 °C. The Au surface was fully covered by the homogeneous AuSi<sub>x</sub> layer. We found that single Si atoms also adsorbed on the B-GNRs (Figure 1c), forming a periodically aligned Si atom array, which is absent on the pristine GNR.<sup>27</sup> This phenomenon can be extended to wider B-GNRs (Figure S1). Since the gap between the adjacent Si atoms is also approximately 1.35 nm (inset of Figure 1c), the Si atom apparently locates at the boron site. Our density functional theory (DFT) calculations indicate that the adsorption energy of 3.71 eV (see Figures 1d,e for the structure) is high enough for Si atom to stay at the site while the substrate was kept at 150 °C during deposition and is about 2 eV more favorable than adsorption at carbon sites. The Si atom adsorbed at the boron site was also observed on the substrate partially covered by the AuSi<sub>x</sub> layer (Figure S2). As shown in Figure 1g, a DFT geometry optimization reveals no major change in the structure of the ribbon when a dense layer of Si atoms is considered between the B-GNR and Au(111) and a tendency of AuSi<sub>x</sub> alloy formation on the Au(111) surface is observed (Figure 1f), as Au atoms are pulled up to the Si layer.

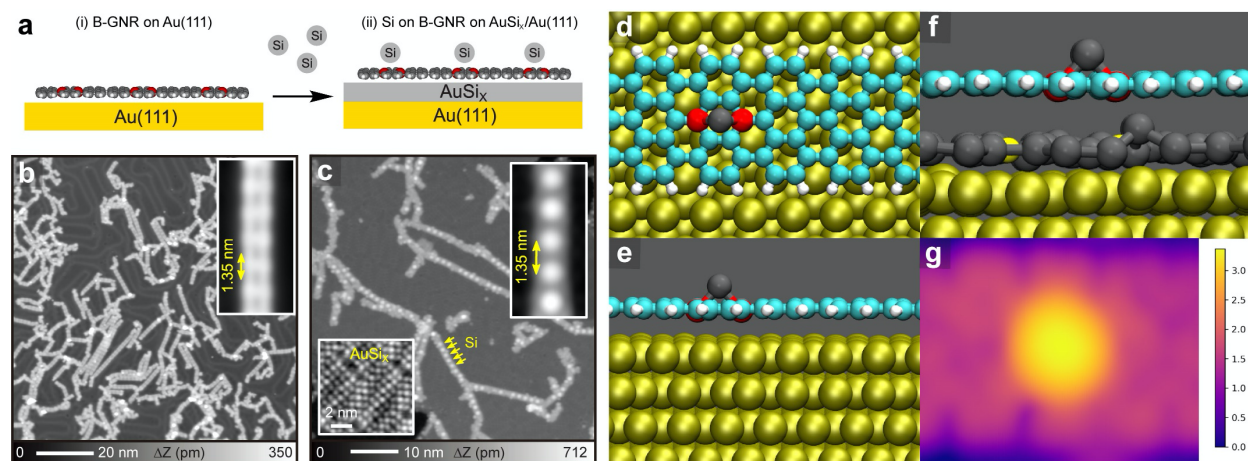


**Figure 1.** (a) Adsorption of Si atoms on B-GNRs formed on a AuSi<sub>x</sub>/Au(111) surface. (b) Large-scale STM topography of B-GNRs formed on Au(111). Inset shows the closeup view of single B-GNR. (c) STM topography after depositing Si atoms on the substrate kept at 150 °C. The lower-left and upper-right insets show closeup views of the atomically resolved AuSi<sub>x</sub> substrate and Si atoms adsorbed on B-GNR, respectively. Simulated structure of Si adsorbed on a B-B site on B-GNR on Au(111) from (d) the top and (e) the side. (f) Same as in (e) but considering a layer of Si atoms between the B-GNR and Au(111). (g) Simulated constant current STM image of structure shown in (f) at a bias of 200 mV.  $\Delta Z$  in the legend is given in Å. Measurement parameters: sample bias voltage  $V = 200$  mV and tunneling current  $I = 3$  pA in (b),  $V = 200$  mV and  $I = 10$  pA in (c).

Since the Si atom strongly binds to the B site and consequently induces a large corrugation amplitude, a significant modification to the electronic properties of B-GNR was expected (Figure S3). Thus, we attempted to remove the Si atom by tip-induced vertical manipulation (Figure 2a). In this process, the  $Z$  feedback of the tunneling junction was deactivated after positioning the tip at the Si site, and subsequently setting the tip closer to the Si atom while recording the tunneling current. Considering the fact that the  $I/V$  converter of the tunneling current was saturated at 10 nA, the tip was set close enough to obtain the single-atom conductance gap and then retracted (Figure

2b). After removing the Si atom, a brick-like contrast appeared around the boron site in the STM topography (Figure 2c), which significantly differs from that of B-GNR directly formed on Au(111) as well as on AuSi<sub>x</sub> layer without any adsorbed Si atom (Figure S4). A systematic scanning tunneling spectroscopy (STS) measurement was conducted at 11 different sites of the B-GNR (Figure 2d). Besides clear peaks at the valence and conduction band edges (Figure S5), distinct zero-bias peaks were measured in the  $dI/dV$  curves taken at the boron sites and their vicinity (Figure 2e). We attributed the peaks to Kondo resonances, arising from the strong interaction between net spin and conduction electrons of the substrate.<sup>22</sup> To further investigate the Kondo resonance, we applied a magnetic field perpendicular to the B-GNR at 4.5 K. The zero-bias peak measured at site 4 became lower and broader with increasing magnetic field, and finally the Zeeman splitting was detected at 12T (Figure 2f). The high magnetic field for the splitting manifests a pair of the spin state of  $S = 1/2$ ,<sup>15</sup> indicating that the apparent zigzag edges caused by the substitution of two boron atoms have no significant magnetic exchange each other. We also obtained temperature dependent zero-bias peaks at the site indicated by blue dot in the bottom-right inset in Figure 2g, with drift-corrected  $dI/dV$  spectroscopy (see method section).<sup>29</sup> The two-dimensional map shows a significant broadening of the zero-bias peak by increasing the temperature (top-left inset in Figure 2g). With Frota fitting, the effective half width at half maximum (HWHM) and the effective temperature  $T_{eff}$  were obtained as scatter plot in Figure 2g. We finally obtained Kondo temperature of  $T_k = 23 \pm 3$  K by fitting with the expression of  $\frac{1}{2}\sqrt{(\alpha k_B T_{eff})^2 + (2k_B T_k)^2}$  (red curve in Figure 2g). The spatial distribution of spin on B-GNR was also shown in the constant height  $dI/dV$  map (Figure 2h) and the two-dimensional maps (Figure S6).

Previous DFT calculations have already demonstrated that imbalanced  $\pi$ -electrons around the pair of B atoms induces a net magnetic moment of  $2 \mu_B$ , which decays towards the segments with only C atoms of the freestanding nanoribbon.<sup>22</sup> Our DFT calculations show that removing one of the adsorbed Si atoms from the freestanding Si-B-GNR also results in a net magnetic moment of  $2\mu_B$  around the pair of boron atoms and is responsible for the Kondo resonances observed in the experiment (Figure 2i and Figure S7). We found no significant ferromagnetic coupling between the apparent zigzag edges, which is consistent with the absence of the side peaks in Figure 2e. The distribution of the spin density in the calculation is in excellent agreement with that in the experiment. We found two important factors for the spin state recovery: (i) Tip-induced Si removal for modification of the local charge state that broke the weak interaction between boron sites and AuSi<sub>x</sub>. In fact, the peak was also absent at the boron sites of GNR on AuSi<sub>x</sub>/Au if no Si atom was a priori adsorbed at the site in the preparation (Figure S8), (ii) AuSi<sub>x</sub> intercalation layer for electronic decoupling. The zero-bias peak was also absent at the boron site of GNR directly adsorbed on Au(111) even if the Si atom was removed by the tip (Figure S9). This implies that the net spin is suppressed due to the strong interaction between boron sites and Au substrate. Overall, this suggests that the B-Si bond scission changes the local charge state around the boron site, which is stabilized by the intercalation layer at low temperature in ultrahigh vacuum. In fact, the spin state at the boron site without a Si atom on AuSi<sub>x</sub>/Au(111) can also be recovered by gentle contact with a Si tip (Figure S10). Given the fact that the system is insensitive to the tip-charging process (Figure S11), the spin state cannot be explained by the triplet ground state biradical caused by two-electron reduction at the boron-doped segment.<sup>30</sup> Rather, it seems that the apparent zigzag edge is responsible.<sup>22</sup> Nevertheless, this result indicates that a combination of the AuSi<sub>x</sub> intercalation layer and the tip-induced removal of a Si atom plays a decisive role in the spin state recovery.

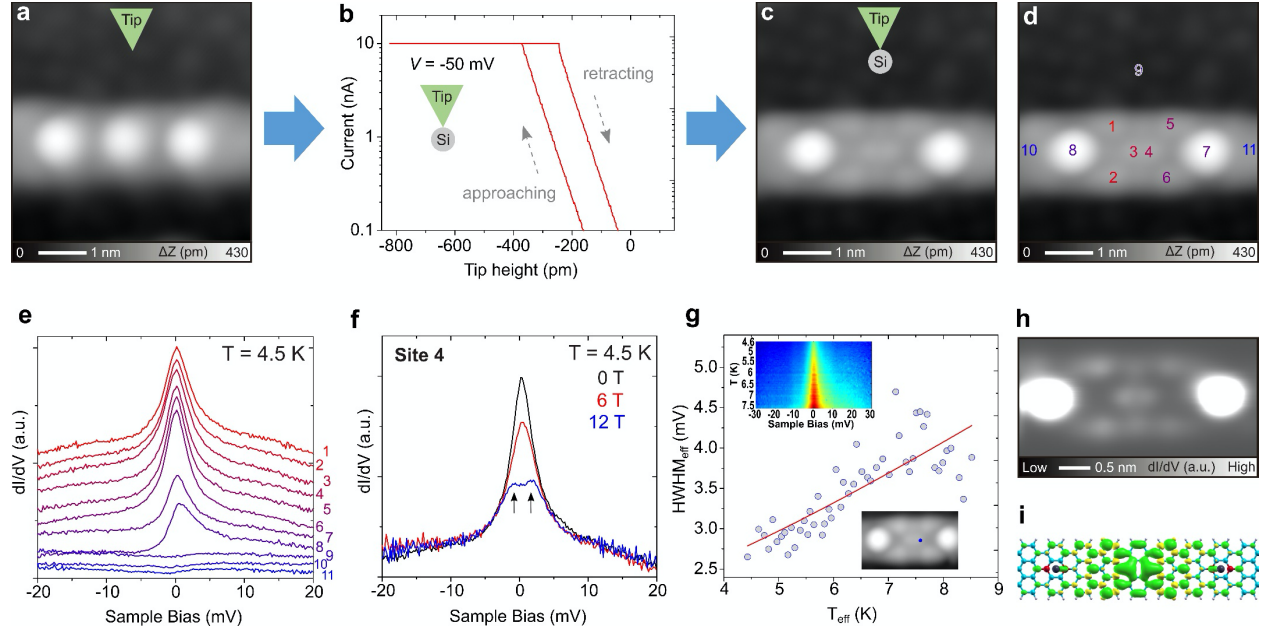


Figure 2. (a) STM topography of the B-GNR formed on  $\text{AuSi}_x/\text{Au}(111)$ . Three Si atoms were adsorbed on the boron sites. (b)  $I$ - $Z$  curve taken during the tip-induced removal of a Si atom. (c) STM topography after the manipulation, and (d) indicating 11 sites for the STS measurement. (e) Corresponding  $dI/dV$  curves measured at 4.5 K. (f)  $dI/dV$  curves recorded in the applied magnetic fields of 0 T (black), 6 T (red), and 12 T (blue). (g) Effective half width at half maximum (HWHM) of Kondo peaks as the function of temperature with fitting curve (red). Insert at the top shows the temperature dependent Kondo resonance (73 curves) measured at the site (indicated by blue dot in the insert at the bottom). (h) Constant height  $dI/dV$  map around the boron site with the recovered spin. (i) DFT calculated spatial distribution of spin. Measurement parameters:  $V = 200$  mV and  $I = 10$  pA in (a), (c), and (d).  $V = 20$  mV,  $I = 400$  pA,  $V_{ac} = 0.5$  mV in (e), (f).  $V = 30$  mV,  $I = 400$  pA,  $V_{ac} = 0.3$  mV in the insert at the top of (g).  $V = 0$  mV,  $V_{ac} = 1.0$  mV in (h).

We further investigated the role of the spin recovery by the tip-induced manipulation and found that magnetism can be transferred along the longitudinal axis of B-GNR by stepwise

removal of Si atoms (Figure 3a). In the process, the half spin polarization ( $S = 1/2$ ) can move through the B-GNR due to the formation of singlet state and creation of new spin states. Figures 3b-f show a series of STM topographies of the B-GNR during the manipulation, in which the apparent width of the GNR becomes larger if the spin exists (Figure S12). The corresponding spatial distribution of spin for Figure 3f was displayed in constant height  $dI/dV$  image (Figure S13). The spin feature moves along with the B-GNR axis following the tip manipulation. The corresponding  $dI/dV$  curves were measured after each STM image (Figures 3g-k). The site hosting the zero-bias peak was shifted by the sequential removal of Si atoms. Note that the zero-bias peak at the edge (black dot) has changed during the process of removing more Si atoms. The specific mechanism is unclear, yet most probably during the process of the Si atom removal by the tip, the interaction between the boron sites and the underlying  $\text{AuSi}_x$  substrate change, resulting in a modification of the zero bias peak. As for the spin transfer, we suggest a plausible mechanism is that spin polarization between neighboring 2B sites can form a closed shell structure, and then the remaining net spin localizes at both ends as indicated by ellipses in Figure 3a.<sup>22</sup> This is supported by the DFT calculations in Figure 3a. Transfer of half spin polarization through the B-GNR has been simulated in the free-standing nanoribbon, which further confirmed the electronic decoupling between the B-GNR and Au(111) by the  $\text{AuSi}_x$  layer. Hence, our results demonstrate the engineering of spin polarization in a single B-GNR.

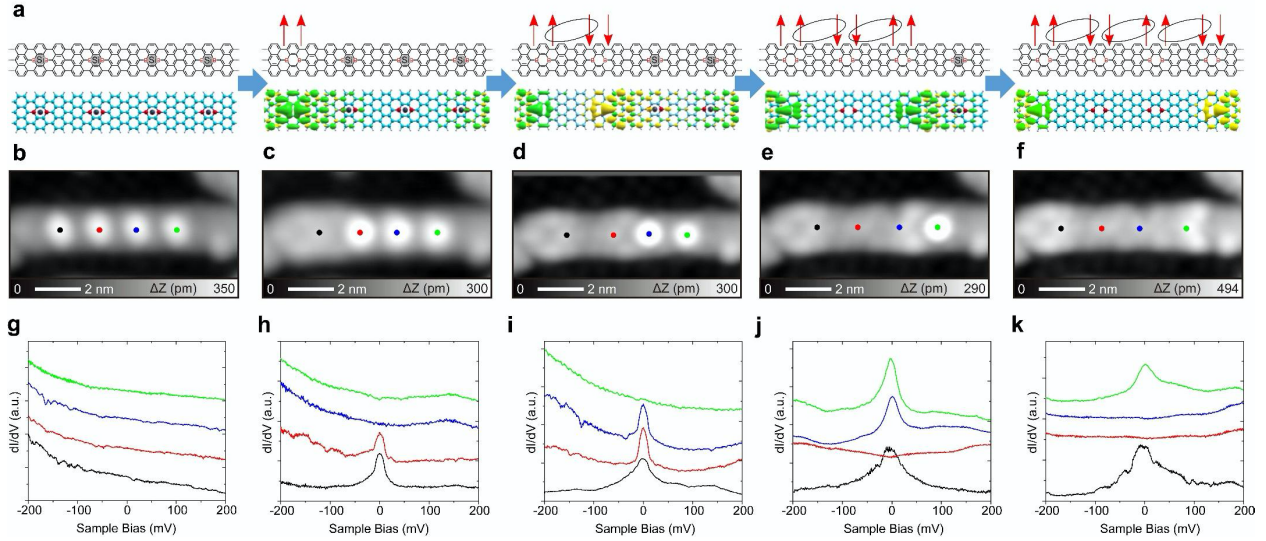


Figure 3. (a) Schematic design and resultant DFT spin densities of the stepwise removal of Si atoms adsorbed on B-GNR by tip-induced manipulation. The green and yellow densities in the DFT calculations are isosurfaces that correspond to spin-up and -down, respectively, where we employed an isovalue of  $4 \times 10^{-4}$  a.u. (b)-(f) STM topographies of B-GNR each after the removal. (g)-(k) Corresponding  $dI/dV$  curves measured at four different sites indicated in (b)-(f). Measurement parameters:  $V = 200$  mV and  $I = 5$  pA for STM.  $V = 200$  mV,  $I = 100$  pA,  $V_{ac} = 10$  mV for STS.

## CONCLUSIONS

We demonstrated real space observation of spin states in B-GNR formed on the  $\text{AuSi}_x/\text{Au}(111)$  surface with low temperature scanning tunneling microscopy. The intercalation layer offers sufficient electronic decoupling, otherwise the magnetic state of B-GNR directly

adsorbed on Au(111) is completely quenched. The tip-induced removal of the silicon atoms adsorbed on the center of two boron sites leads to the recovery of a net spin in the corresponding two-boron site. Our DFT calculations demonstrate that the spin state is recovered on the pair of B atoms when the adsorbed Si atom is removed in the free standing B-GNR, thus confirming the decoupling from the Au(111) substrate by the  $\text{AuSi}_x$  buffer layer in the experiment. This manipulation process can be repeated with an effective transfer of the spin site along the longitudinal axis of B-GNR, resulting in local-probe spin engineering. We hope that this demonstration will offer a route to the control of the spin state in quantum materials.

## Methods/Experimental

**Experimental Section:** All the experiments were conducted with two scanning tunneling microscopy (STM) systems under ultra-high vacuum environment: a home-made STM operating at 4.3 K ( $< 1 \times 10^{-10}$  mbar), and a Unisoku STM operating at 4.5 K ( $< 1 \times 10^{-10}$  mbar) with a maximum out-of-plane magnetic field of 16 T. Clean Au(111) substrates were prepared by cyclic  $\text{Ar}^+$  sputtering for 10 min and annealing at 440 °C for 10 min. 9,10-bis(10-bromoanthracen-9-yl)-9,10-dihydro-9,10-diboraanthracene molecules were deposited on Au(111) kept at room temperature from crucibles of a Knudsen cell, heated at approximately 250 °C. The sample was heated to 180 °C for debromination and 320 °C for cyclodehydrogenation, resulting in formation of boron substituted graphene nanoribbons (B-GNRs). Silicon atoms were deposited by a one-pocket electron beam evaporator (SPECS GmbH) on B-GNRs/Au(111) kept at 150 °C for fabrication of B-GNRs with adsorbed Si atoms and an  $\text{AuSi}_x$  buffer layer. STM tungsten tips were made by chemical etching. The modulation amplitude was 10  $\text{mV}_{\text{ac}}$  and 0.3  $\text{mV}_{\text{ac}}$  with the

frequency 510 Hz for STS measurement in home-made STM system. The modulation amplitude was 0.5 mV<sub>ac</sub> and the frequency was 830 Hz for STS measurement in Unisoku STM system. Before the temperature dependent  $dI/dV$  spectroscopic measurements, the liquid helium in the cryostat was fully evaporated. Then, the temperature was gradually increased. The non-linear thermal drifts in the X, Y, and Z directions were thoroughly corrected by drift-corrected  $dI/dV$  spectroscopy. Before each  $dI/dV$  measurements, the tip was repositioned at the adjacent site of the Si atom adsorbed on the boron site of B-GNR, by activating an atom tracking function for 120 sec. The recorded travels of the thermal drifts in the X, Y, and Z directions during the atom tracking were used for the feedforward compensation during the next spectroscopic measurement. A similar protocol can be found in Ref 29.

A small amount of Si atoms were deposited on Au(111) kept at 150 °C for homogeneous adsorption on B-GNR (Figure S2a). Some uniformly-spaced bright dots can be seen on B-GNRs in STM image (Figure S2b), which are identified as Si atoms. Insert (Figure S2b) shows a closeup of one B-GNR with adsorbed Si atoms, in which the gap between neighboring Si atoms is  $1.34 \pm 0.01$  nm, the same as the periodic distance in pure B-GNR within the allowed error range. Some small dark areas on Au(111) could be seen, which are identified as AuSi<sub>x</sub> regions, consistent with recent research.<sup>27,28</sup>

**Computational section:** All first-principles calculations on the gold substrate in this work were performed using the periodic plane-wave basis VASP code<sup>31,32</sup> implementing the spin-polarized Density Functional Theory. To accurately include van der Waals interactions in this system, we used the DFT-D3 method with Becke-Jonson damping.<sup>33,34</sup> Projected augmented wave potentials were used to describe the core electrons<sup>35</sup> with a kinetic energy cutoff of 500 eV (with PREC = accurate). Systematic  $k$ -point convergence was checked for all systems with sampling

chosen according to the system size. This approach converged the total energy of all the systems to the order of 1 meV. The properties of the bulk and surface of Au were carefully checked within this methodology, and excellent agreement was achieved with experiments. For calculations of the ribbons on the surface, a vacuum gap of at least 1.5 nm was used, and the size of the gold slab ( $6\times 6$  units cells) and ribbon length ( $4\times 1$ ) were chosen to minimize the lattice mismatch (1.4% for this combination). A  $5\times 5\times 1$   $k$ -point grid was used and the upper three layers of Au (five layers in total) and all atoms in the ribbon were allowed to relax to a force of less than  $0.01$  eV/Å. All energies mentioned are with reference to relaxed total energies. Atomic structure visualizations were made with the VMD package.<sup>36</sup> Simulated STM images were calculated using the CRITIC2 package<sup>37,38</sup> based on the Tersoff-Hamann approximation.<sup>39</sup>

In order to explore the development of the magnetic properties of the B-GNR with Si atoms adsorbed, we used the VASP relaxed structure as input for calculations of much longer ribbons. In Figure S7 is shown an example of ribbon which has two pairs of boron atoms with Si adsorbed and one pair without the Si. This calculation was realized without any substrate in order to simulate the decoupling of the B-GNR with the Au substrate intermediated by the  $\text{AuSi}_x$  layer. For these simulations we have made use of the SIESTA code<sup>40,41</sup> with the vdW functional of Dion *et al*<sup>42</sup> with exchange modified by J. Klimeš, D. R. Bowler, and A. Michaelides (KBM, also known as optB88-vdW functional).<sup>43</sup> The fineness of the real reciprocal space integration was defined by an energy cutoff of 300 Ry, while the reciprocal space was sampled with a  $2\times 1\times 1$  Monkhorst-Pack grid.<sup>44</sup> Norm conserving Troullier-Martins pseudopotentials were used to represent the ionic core potentials,<sup>45</sup> while a double- $\zeta$  plus polarization (DZP) basis set is adopted for the valence electrons. The optimized geometry was achieved after the magnitude of the largest force on the atoms was smaller than  $0.01$  eV/Å, and two vacuum layers, perpendicular and parallel to the ribbons, of 1.5

nm were considered so that the interaction between the ribbons were negligible. The threshold for the self-consistency cycle was set to  $10^{-5}$  eV to the density matrix elements and  $10^{-2}$  eV for the Hamiltonian matrix elements.

## **ASSOCIATED CONTENT**

### **Supporting Information.**

The following files are available free of charge at <https://pubs.acs.org/doi/.....>

Further details of the experimental and theoretical calculation procedures, additional experimental and theoretical data (PDF).

## **AUTHOR INFORMATION**

### **Corresponding Author**

\* adam.foster@aalto.fi

\* Kawai.shigeki@nims.go.jp

## **ORCID**

Kewei Sun: 0000-0002-1835-243X

Orlando J. Silveira: 0000-0002-0403-9485

Shohei Saito: 0000-0003-1863-9956

Keisuke Sagisaka: 0000-0002-5089-4271

Shigehiro Yamaguchi: 0000-0003-0072-8969

Adam S. Foster: 0000-0001-5371-5905

Shigeki Kawai: 0000-0003-2128-0120

### **Author Contributions**

S.K. conceived the project and supervised the STM measurement. K. Sun performed the STM measurement. For the magnetic measurement, K. Sagisaka supervised K. Sun. O.J.S. and A.S.F. carried out the theoretical calculations. S.S. and S.Y synthesized the precursor molecules. K.Sun, O.J.S., A.S.F., and S.K wrote the manuscript and all the authors discussed the results.

### **Notes**

The authors declare no competing financial interest.

### **ACKNOWLEDGMENTS**

This work was supported in part by Japan Society for the Promotion of Science (JSPS) KAKENHI Grant Number 21F21058 and 21K18885, and 22H00285. Computing resources from the Aalto Science-IT project and CSC, Helsinki are gratefully acknowledged. A.S.F. has been supported by the World Premier International Research Center Initiative (WPI), MEXT, Japan. K.Sun thanks S. Yoshizawa for his technical support in the STM measurement in the magnetic field.

### **REFERENCES**

1. Fernández-Rossier, F.; Palacios, J. J. Magnetism in graphene nanoislands. *Phys. Rev. Lett.* **2007**, *99*, 177204.

2. Pesin, D.; MacDonald, A. H. Spintronics and Pseudospintronics in Graphene and Topological Insulators. *Nat. Mater.* **2012**, *11*, 409-416.
3. Grill, L.; Dyer, M.; Lafferentz, L.; Persson, M.; Peters, M. V.; Hecht, S. Nano-Architectures by Covalent Assembly of Molecular Building Blocks. *Nat Nanotechnol.* **2007**, *2*, 687-691.
4. Grill, L.; Hecht, S. Covalent On-Surface Polymerization. *Nat. Chem.* **2020**, *12*, 115-130.
5. Talirz, L.; Ruffieux, P.; Fasel, R. On-Surface Synthesis of Atomically Precise Graphene Nanoribbons. *Adv Mater.* **2016**, *28*, 6222-6231.
6. Cai, J.; Ruffieux, P.; Jaafar, R.; Bieri, M.; Braun, T.; Blankenburg, S.; Muoth, M.; Seitsonen, A. P.; Saleh, M.; Feng, X.; Müllen, K.; Fasel, R. Atomically Precise Bottom-Up Fabrication of Graphene Nanoribbons. *Nature* **2010**, *466*, 470-473.
7. Treier, M.; Pignedoli, C. A.; Laino, T.; Rieger, R.; Müllen, K.; Passerone, D.; Fasel, R. Surface-Assisted Cyclodehydrogenation Provides a Synthetic Route Towards Easily Processable and Chemically Tailored Nanographenes. *Nat Chem.* **2011**, *3*, 61-67.
8. Ruffieux, P.; Wang, S.; Yang, B.; Sanchez-Sanchez, C.; Liu, J.; Dienel, T.; Talirz, L.; Shinde, P.; Pignedoli, C. A.; Passerone, D.; Dumlaff, T.; Feng, X.; Müllen, K.; Fasel, R. On-Surface Synthesis of Graphene Nanoribbons with Zigzag Edge Topology. *Nature* **2016**, *531*, 489-492.
9. Gröning, O.; Wang, S.; Yao, X.; Pignedoli, C. A.; Borin Barin, G.; Daniels, C.; Cupo, A.; Meunier, V.; Feng, X.; Narita, A.; Müllen, K.; Ruffieux, P.; Fasel, R. Engineering of Robust Topological Quantum Phases in Graphene Nanoribbons. *Nature* **2018**, *560*, 209-213.
10. Rizzo, D. J.; Veber, G.; Cao, T.; Bronner, C.; Chen, T.; Zhao, F.; Rodriguez, H.; Louie, S. G.; Crommie, M. F.; Fischer, F. R. Topological Band Engineering of Graphene Nanoribbons. *Nature* **2018**, *560*, 204-208.

11. Sun, Q.; Yao, X.; Gröning, O.; Eimre, K.; Pignedoli, C. A.; Müllen, K.; Narita, A.; Fasel, R.; Ruffieux, P. Coupled Spin States in Armchair Graphene Nanoribbons with Asymmetric Zigzag Edge Extensions. *Nano Lett.* **2020**, *20*, 6429–6436.
12. Rizzo, D. J.; Veber, G.; Jiang, J.; McCurdy, R.; Cao, T.; Bronner, C.; Chen, T.; Louie, S. G.; Fischer, F. R.; Crommie, M. F. Inducing Metallicity in Graphene Nanoribbons via Zero-Mode Superlattices. *Science* **2020**, *369*, 1597–1603.
13. Li, J.; Sanz, S.; Corso, M.; Choi, D.; Pena, D.; Frederiksen, T.; Pascual, J. I. Single Spin Localization and Manipulation in Graphene Open-Shell Nanostructures. *Nat. Commun.* **2019**, *10*, 200.
14. Pavliček, N.; Mistry, A.; Majzik, Z.; Moll, N.; Meyer, G.; Fox, D. J.; Gross, L. Synthesis and Characterization of Triangulene. *Nat. Nanotechnol.* **2017**, *12*, 308–311.
15. Mishra, S.; Beyer, D.; Eimre, K.; Kezilebieke, S.; Berger, R.; Gröning, O.; Pignedoli, C. A.; Müllen, K.; Liljeroth, P.; Ruffieux, P.; Feng, X.; Fasel, R. Topological Frustration Induces Unconventional Magnetism in a Nanographene. *Nat. Nanotechnol.* **2020**, *15*, 22–28.
16. Mishra, S.; Beyer, D.; Berger, R.; Liu, J.; Gröning, O.; Urgel, J. I.; Müllen, K.; Ruffieux, P.; Feng, X.; Fasel, R. Topological Defect-Induced Magnetism in a Nanographene. *J. Am. Chem. Soc.* **2020**, *142*, 1147–1152.
17. Li, J.; Sanz, S.; Castro-Esteban, J.; Vilas-Varela, M.; Friedrich, N.; Frederiksen, T.; Pena, D.; Pascual, J. I. Uncovering the Triplet Ground State of Triangular Graphene Nanoflakes Engineered with Atomic Precision on a Metal Surface. *Phys. Rev. Lett.* **2020**, *124*, 177201.
18. Zheng, Y.; Li, C.; Zhao, Y.; Beyer, D.; Wang, G.; Xu, C.; Yue, X.; Chen, Y.; Guan, D. D.; Li, Y. Y.; Zheng, H.; Liu, C.; Luo, W.; Feng, X.; Wang, S.; Jia, J. Engineering of Magnetic Coupling in Nanographene. *Phys. Rev. Lett.* **2020**, *124*, 147206.

19. Zheng, Y.; Li, C.; Xu, C.; Beyer, D.; Yue, X.; Zhao, Y.; Wang, G.; Guan, D.; Li, Y.; Zheng, H.; Liu, C.; Liu, J.; Wang, X.; Luo, W.; Feng, X.; Wang, S.; Jia, J. Designer Spin Order in Diradical Nanographenes. *Nat. Commun.* **2020**, *11*, 6076.
20. Su, J.; Telychko, M.; Hu, P.; Macam, G.; Mutombo, P.; Zhang, H.; Bao, Y.; Cheng, F.; Huang, Z.-Q.; Qiu, Z.; Tan, S. J. R.; Lin, H.; Jelínek, P.; Chuang, F.-C.; Wu, J.; Lu, J. Atomically Precise Bottom-Up Synthesis of  $\pi$ -Extended [5]Triangulene. *Sci. Adv.* **2019**, *5*, eaav7717.
21. Wang, S.; Talirz, L.; Pignedoli, C. A.; Feng, X.; Müllen, K.; Fasel, R.; Ruffieux, P. Giant Edge State Splitting at Atomically Precise Graphene Zigzag Edges. *Nat. Commun.* **2016**, *7*, 11507.
22. Friedrich, N.; Brandimarte, P.; Li, J.; Saito, S.; Yamaguchi, S.; Pozo, I.; Pena, D.; Frederiksen, T.; Garcia-Lekue, A.; Sanchez-Portal, D.; Pascual, J. I. Magnetism of Topological Boundary States Induced by Boron Substitution in Graphene Nanoribbons. *Phys. Rev. Lett.* **2020**, *125*, 146801.
23. Kawai, S.; Saito, S.; Osumi, S.; Yamaguchi, S.; Foster, A. S.; Spijker, P.; Meyer, E. Atomically Controlled Substitutional Boron-Doping of Graphene Nanoribbons. *Nat. Commun.* **2015**, *6*, 8098.
24. Carbonell-Sanromà, E.; Brandimarte, P.; Balog, R.; Corso, M.; Kawai, S.; Garcia-Lekue, A.; Saito, S.; Yamaguchi, S.; Meyer, E.; Sánchez-Portal, D.; Pascual, J. I. Quantum Dots Embedded in Graphene Nanoribbons by Chemical Substitution. *Nano Lett.* **2017**, *17*, 50-56.
25. Kawai, S.; Benassi, A.; Gnecco, E.; Söde, H.; Pawlak, R.; Müllen, K.; Passerone, D.; Pignedoli, C.; Ruffieux, P.; Fasel, R.; Meyer, E. Superlubricity of Graphene Nanoribbons on Gold Surfaces. *Science* **2016**, *351*, 957-961.

26. Carbonel-Sanroma, E.; Garcia-Lekue, A.; Corso, M.; Vasseur, G.; Brandimarte, P.; Lobo, J.; de Oteyza, D. G.; Li, J.; Kawai, S.; Saito, S.; Yamaguchi, S.; Ortega, J. E.; Sanchez-Portal, D.; Pascual, J. I. Electronic Properties of Substitutionally Boron-Doped Graphene Nanoribbons on Au(111) Surface. *J. Phys. Chem. C* **2018**, *122*, 16092-16099.
27. Deniz, O.; Sanchez-Sanchez, C.; Dumsclaff, T.; Feng, X.; Narita, A.; Müllen, K.; Kharche, N.; Meunier, V.; Fasel, R.; Ruffieux, P. Revealing the Electronic Structure of Silicon Intercalated Armchair Graphene Nanoribbons by Scanning Tunneling Spectroscopy. *Nano Lett.* **2017**, *17*, 2197-2203.
28. Sun, K.; Kawai, S. Strength of Electronic Decoupling of Fullerene on an AuSi<sub>x</sub> Layer Formed on Au(111). *Phys. Chem. Chem. Phys.* **2021**, *23*, 5455-5459.
29. Kawai, S.; Glatzel, T.; Koch, S.; Baratoff, A.; Meyer, E. Interaction-Induced Atomic Displacements Revealed by Drift-Corrected Dynamic Force Spectroscopy. *Phys Rev B* **2011**, *83*, 035421.
30. Osumi, S.; Saito, S.; Dou, C.; Matsuo, K.; Kume, K.; Yoshikawa, H.; Awaga, K.; Yamaguchi, S. Boron-Doped Nanographene: Lewis Acidity, Redox, Properties, and Battery Electrode Performance. *Chem. Sci.* **2016**, *7*, 219-227.
31. Kresse, G.; Furthmüller, J. Efficiency of ab-initio Total Energy Calculations for Metals and Semiconductors Using a Plane-Wave Basis Set. *Comp. Mat. Sci.* **1996**, *6*, 15–50.
32. Kresse, G.; Furthmüller, J. Efficient Iterative Schemes for ab initio Total-Energy Calculations Using a Plane-Wave Basis Set. *Phys. Rev. B* **1996**, *54*, 11169–11186.
33. Grimme, S.; Antony, J.; Ehrlich, S.; Krieg, S. A Consistent and Accurate *ab initio* Parametrization of Density Functional Dispersion Correction (DFT-D) for the 94 Elements H-Pu. *J. Chem. Phys.* **2010**, *132*, 154104.

34. Grimme, S.; Ehrlich, S.; Goerigk, L. Effect of the Damping Function in Dispersion Corrected Density Functional Theory. *J. Comp. Chem.* **2011**, *32*, 1456–1465.
35. Blochl, P. E. Projector Augmented-Wave Method. *Phys. Rev. B* **1994**, *50*, 17953–17979.
36. Humphrey, W.; Dalke, A.; Schulten, K. VMD: Visual Molecular Dynamics. *J. Mol. Graphics* **1996**, *14*, 33–38.
37. Otero-de-la-Roza, A.; Blanco, M. A.; Pendás, A. M.; Luaña, V. Critic: A New Program for the Topological Analysis of Solid-State Electron Densities. *Comput. Phys. Commun.* **2009**, *180*, 157–166.
38. Otero-de-la-Roza, A.; Johnson, E. R.; Luaña, V. CRITIC2: A program for Real-Space Analysis of Quantum Chemical Interactions in Solids. *Comput. Phys. Commun.* **2004**, *185*, 1007-1018.
39. Tersoff, J.; Hamann, D. R. Theory of the Scanning Tunneling Microscope. *Phys. Rev. B* **1985**, *31*, 805–813.
40. Soler, J. M.; Artacho, E.; Gale, J. G.; García, A.; Junquera, J.; Ordejón, P.; Sánchez-Portal, D. The SIESTA Method for *ab initio* Order-*N* Materials Simulation. *J. Phys.: Condens. Matter* **2002**, *14*, 2745.
41. García, A.; Papior, N.; Akhtar, A.; Artacho, E.; Blum, V.; Bosoni, E.; Brandimarte, P.; Brandbyge, M.; Cerdá, J. I.; Corsetti, F.; Cuadrado, R.; Dikan, V.; Ferrer, J.; Gale, J.; García-Fernández, P.; García-Suárez, V. M.; García, S.; Huhs, G.; Illera, S.; Korytár, R.; Koval, P.; Lebedeva, I.; Lin, L.; López-Tarifa, P.; Mayo, S. G.; Mohr, S.; Ordejón, P.; Postnikov, A.; Pouillon, Y.; Pruneda, M.; Robles, R.; Sánchez-Portal, D.; Soler, J. M.; Ullah, R.; Yu, V. W.-z.; Junquera, J. SIESTA: Recent Developments and Applications. *J. Chem. Phys.* **2020**, *152*, 204108.

42. Dion, M.; Rydberg, H.; Schröder, E.; Langreth, D. C.; Lundqvist, B. I. Van der Waals Density Functional for General Geometries. *Phys. Rev. Lett.* **2001**, *92*, 246401.
43. Klimeš, J.; Bowler, D. R.; Michaelides, A. J. Chemical Accuracy for the Van der Waals Density Functional. *Phys.: Condens. Matter* **2010**, *22*, 022201.
44. Monkhorst, H. J.; Pack, J. D. Special Points for Brillouin-Zone Integrations. *Phys. Rev. B.* **1976**, *13*, 5188–5192.
45. Troullier, N.; Martins, J. L. Efficient Pseudopotentials for Plane-Wave Calculations. *Phys. Rev. B* **1991**, *43*, 1993–2006.

## Table of Contents

